Advanced Electronic Materials

www.advelectronicmat.de

RESEARCH ARTICLE OPEN ACCESS

Metal–Insulator–Insulator–Metal (MIIM) Ag/SnO_2/Al_2O_3/Ag Diodes Fabricated by Ultraprecise Dispensing and Atomic Layer Deposition

Aboubacar Savadogo[1,2] | Klaus Huska[1] | Rohit D. Chavan[1] | Thomas Nyachoti Nyangonda[2] | Jan Feßler[1] | Bernard Odhiambo Aduda[2] | Ulrich Wilhelm Paetzold[1,3] | Uli Lemmer[1,3] | Mohamed Hussein[1,4]

[1]Light Technology Institute (LTI), Karlsruhe Institute of Technology (KIT), Karlsruhe, Germany | [2]Department of Physics, University of Nairobi, Nairobi, Kenya | [3]Institute of Microstructure Technology (IMT), Karlsruhe Institute of Technology (KIT), Eggenstein-Leopoldshafen, Germany | [4]Department of Physics, Faculty of Science, Ain Shams University, Abbassia, Cairo, Egypt

Correspondence: Aboubacar Savadogo (aboubacar.savadogo@partner.kit.edu) | Uli Lemmer (ulrich.lemmer@kit.edu) | Mohamed Hussein (mohamed.hussein@kit.edu)

Received: 8 September 2025 | **Revised:** 4 January 2026 | **Accepted:** 5 January 2026

Keywords: metal–insulator–insulator–metal (MIIM) diode | rectenna | responsivity | ultra-precise dispensing | wentzel-kramers-brillouin (WKB)

ABSTRACT

Currently, high-frequency, ultra-fast, and tunneling diodes are mainly fabricated using traditional lithography and evaporation techniques, typically limited to wafer sizes. This work introduces a new method for fabricating metal–insulator–insulator–metal (MIIM) diodes using ultra-precise dispensing (UPD) printing techniques, providing a practical alternative to traditional lithography. Enabling highly precise material deposition, minimizing waste and boosting manufacturing efficiency. Both bottom and top electrodes of the MIIM diode are silver(Ag) and fabricated via UPD, while atomic layer deposition (ALD) is employed to deposit the insulating layers. 1 nm of tin oxide(SnO_2) and 1 nm of aluminum oxide(Al_2O_3) sandwiched between the electrodes: The Ag/SnO_2/Al_2O_3/Ag MIIM diode has a contact area of ca. 5.4 µm × 4.0 µm determined by FIB-SEM. A quantum simulator based on the Wentzel-Kramers-Brillouin (WKB) method is used to analyze the diode's performance and shows agreement with measurement results. The electrical characterization of the fabricated MIIM device exhibits a tunneling current in the nano- to microampere range, a zero-bias responsivity of −1.31 A/W, and dynamic resistance of 39.56 kΩ. Combining ultra-precise printing with innovative insulators provides a promising pathway to large-scale, low-cost production of high-performance MIM diodes for energy harvesting, high-frequency rectification, and flexible applications electronics.

1 | Introduction

Terahertz (THz) rectification is essential for realizing rectennas that harvest infrared radiation, enable imaging through thermal emission detection, and convert solar energy [1]. Rectennas also show significant potential in wireless THz communications, especially in satellite systems, where their large bandwidth capacity (up to 100 GHz) could support data transfer rates exceeding 1 Gb/s. Further, they can serve as detectors for THz biomedical imaging, including applications like skin cancer diagnostics and passive imaging systems [2]. The rectennas have an ability to recycle residual heat, whether produced by small electronic devices, combustion engines, or large industrial machinery. Despite this potential, developing rectennas that operate at higher IR/THz frequencies remains challenging due to the lack of THz diode structures that couple efficiently with antennas. Metal–Insulator–Insulator–Metal (MIIM) tunneling diodes are promising for these applications [3, 4], and they have demonstrated potential for THz rectification, especially when integrated into rectenna systems [5–7].

The MIM diodes are gaining increasing attention in nanoscale energy harvesting due to their high-frequency rectification and ultra-fast response. Double-dielectric architectures (MIIM diodes) can further enhance their rectification ability. IR/THz rectenna rectification relies on ultrafast tunneling with low turn-on voltages ideally near zero bias to enable efficient energy harvesting operation in rectenna arrays [8]. These quantum tunneling devices offer advantages over traditional Schottky diodes in applications such as ambient radio-frequency (RF) energy harvesting, infrared rectennas, and wireless power transfer systems, especially when low leakage current and high rectification ratios are essential [8].

The performance of MIIM diodes depends on the selection and combination of electrodes and insulators, as well as the fabrication method. Typically, fabrication relies on conventional thin film deposition techniques such as e-beam evaporation [9–11] or atomic layer deposition(ALD) [12, 13], combined with photolithography [14] and etching. Although these methods offer precise control over thickness and uniformity, they are often expensive, complex, and unsuitable for flexible or large-area substrates [15, 16]. Furthermore, their batch processing approach limits rapid fabrication and cost-effective mass production. Recently, advances in ultra-precise printing technologies—such as electrohydrodynamic (EHD) jet printing, aerosol jet printing, and nanoscale inkjet deposition offer promising alternatives in MIIM diode manufacturing. These additive techniques enable direct-write patterning of functional materials with sub-micron high spatial resolution, high material efficiency, and compatibility with temperature-sensitive and flexible substrates [17]. When adapted for MIIM structures, these methods enable layer-by-layer deposition of metal and dielectric inks, providing precise control over tunneling barrier thickness and device geometry crucial for improving energy harvesting performance. Additionally, printed MIIM diodes introduced in this paper have shown potential for RF energy harvesting at terahertz frequencies due to their low capacitance and fast tunneling response [18]. Producing these devices with precise spatial control and material selectivity via scalable printing methods significantly reduces manufacturing costs. It enables integration into flexible, wearable, or distributed power systems. In this context, ultra-precise dispensing (UPD) technology (XTPL S.A.) is a direct ink writing (DIW) technique suitable for additive manufacturing of electronic devices. The inks contain no toxic substances, and the manufacturing relies on a high-precision, single-step process [19]. It uses a high-viscosity ink (>10^5 mPa·s) in contact with the substrate, enabling high-precision printing [20]. Thus, the amount of deposited ink is well controlled, enabling its use for fabricating conductive interconnects and making the process waste-free [21]. The UPD method and its applications in electronics are explained in [16, 22]. The XTPL delta printer provides high precision, achieving the single-micrometer range with the smallest available nozzle of 1.5 µm (internal opening) [19, 23].

This paper presents a novel approach for MIIM diode fabrication using UPD, highlighting its potential in energy-harvesting applications. On the other hand, in this study, we demonstrate a new method for fabricating MIIM diodes by combining the UPD printing technique with ALD. This approach aims to overcome the limitations of traditional lithography-based processes in large-scale reproducibility, fabrication costs, and compatibility with unconventional substrates. By enabling high-resolution localized material deposition, UPD offers a versatile, potentially more cost-effective pathway for producing MIIM structures. Table 1 in the manuscript compares previous studies on Metal-Insulator(s)-Metal diodes, including both single- and multiple-insulator layers, and highlights different fabrication techniques based on their figures of merit. The manuscript is organized as follows: Section 2 covers the device fabrication and simulation methodology, Section 3 discusses the results and discussion, and Section 4 provides the conclusion.

2 | Methods

2.1 | MIIM Diode Design

We here report an MIIM diode comprising two insulator layers: aluminum oxide (Al_2O_3) and tin oxide (SnO_2), sandwiched between two printed silver (Ag) electrodes that work as the bottom and top contacts, as shown in Figure 1a. The choice of combining these materials is motivated by the fact that Al_2O_3 is known as a perfect insulating layer, and SnO_2 surpasses other ultrathin oxide materials (TiO_2, ZnO, HfO_2, MgO). Because it provides optimal electron affinity, a low barrier height, pinhole-free growth at sub-nanometer thickness, low defect density, and stable band alignment that enable efficient quantum tunneling [35, 36]. It has also been used in [32] as an insulating material. The polar discontinuities at the interfaces further contribute to the generation and/or removal of charge carriers. Moreover, Hupp et al. [37] demonstrated in their experiments that depositing 1 nm ALD Al_2O_3 followed by ALD SnO_2 creates a well-defined, uniform surface with improved interface quality, resulting in a smooth, uniform, and pinhole-free surface. Additionally, among the widely used electrode materials, Ag showed the highest efficiencies, with radiation efficiencies exceeding 90%, outperforming gold (Au) and aluminum (Al) [38].

The energy band diagram of the MIIM structure is shown in Figure 1b. Indeed, under positive bias as depicted in Figure 1c, resonant tunneling (RT) can occur in double-barrier MIIM structures when the quantum well formed between the dielectrics becomes wide and deep enough to support bound states [28]. Conventional tunneling through the Al_2O_3 occurs (Figure 1d) when the metal Fermi level on the higher barrier side rising above the conduction band of the lower barrier, thereby reducing the tunneling distance.

The tunneling current is theoretically described by Equation (1) as in [31, 39].

$$I(V) = (4\pi me/h^3)\ \int_0^\infty T(E_x)dE_x \int_{E_x}^\infty \{f_L(E) - f_R(E + eV_D)\}\, dE \tag{1}$$

where, $T(E_x) \approx \exp(-2/h \int_a^b \sqrt{2m(-eV(x) - E)}dx)$ represents the tunneling probability based on the Wentzel-Kramers-Brillouin (WKB) method, h is Planck's constant, m is the mass of the electron, e is the elementary charge, $f_L(E)$ and $f_R(E + eV_D)$ are the Fermi levels of each base metal, -eV(x) is the spatially

TABLE 1 | Comparison between some previous works done on Metal-Insulator(s)-Metal diodes with single and multiple using different fabrication techniques.

Refs.	Diode	β_0 [A/W]	R_D [Ω]	Area [μm^2]	Fabrication techniques (Insulator/Electrodes)
This work	Ag/SnO_2(1 nm) /Al_2O_3(1 nm)/Ag	−1.31	39.56 K	5.4×4	ALD/DIW (ultra-precise dispensing)
[24]	Al/Sc_2O_3(3 nm) /Al Au/Al_2O_3(3 nm) /Au	1 0.08	0.96 M 58.2M	100×100 100×100	NanoPVD-RF magnetron sputter / thermal evaporation ALD/ thermal evaporation
[25]	Ni/NiO(>4 nm)/Ni	−0.41	42.4M	0.018	Plasma oxidation/e-BEAM WRITING
[26]	Au/ Al_2O_3(3 nm)/Au Nb_2O_5(1 nm)/Ta_2O_5(3 nm)//Al_2O_3(1 nm)/Al	0.1 −3.7	83 M 3.6G	100×100	ALD/ thermal evaporation
[27]	V/V_2O_5(1.45 nm)/V	—	13.4 K	2×2	RF Sputtering /Electron-beam lithography-sputtering
[28]	Al/Al_2O_3(1 nm)/Nb_2O_5(3–6 nm)/Al	—	—		Sputtering ALD/thermal evaporation
[29]	Pt/ZnO(2.5–9.5 nm)/Al_2O_3(2.5–13 nm)/Al	12	—	10×10	AP-CVD/deposition via photolithography
[30]	Ag/HfO_2(4 nm) /Al_2O_3(4 nm) /Au	0.00641	18.7 K	$2.10^4 \times 2.10^4$	Atomic deposition/Spin coating-atomic deposition
[3]	PolySi/SiO_2(1.38 nm)/Au	~1.25	120 M	0.35	Boiling water oxidation/ e-beam writing
[31]	Au/ZnO(2 nm)/SiO_2(2 nm)Al_2O_3(2 nm) /Al	−11.7	420M	5000	ALD/ lithography-sputtering
[32]	Cr/SnO_2(20 nm)//NiO(10 nm)//Cr	—	—	—	E-Beam Evaporation
[33]	Al/ Al_2O_3(~2 nm)/ Ti Al/ Al_2O_3(~2 nm)/ Pt	0.6 1	— —	~0.05×0.05	Oxidation/E-beam lithography-Evaporation
[34]	Al/ Al_2O_3(1–2 nm)/ Pt	0.0012	124.6	~0.080×0.1	Oxidation/E-beam lithography-Evaporation

dependent conduction band minimum of the insulating layer, and the integration upper and lower limits |a-b| represent the effective tunnel distance when bias is applied.

With multi-insulators, as is the case here, with different affinities and bandgaps, different barriers are created at the metal–insulator and insulator–insulator interfaces between Ag/SnO_2, SnO_2/Al_2O_3, and Al_2O_3/Ag. The electron affinities of the ALD-deposited SnO_2 and Al_2O_3 are 4.5 eV (χ_1) and 1.57 eV (χ_2), respectively. The work function of the Ag was $\varphi_1 = 4.7\, eV$. Therefore, the barrier heights were calculated as follows: $\varnothing_1 = \varphi_1 - \chi_1 = 0.2$ eV, $\varnothing_2 = \chi_1 - \chi_2 = 2.93$ eV and $\varnothing_3 = \varphi_1 - \chi_2 = 3.13$ eV. Then, we observe from the diagrams in Figure 1c,d that resonant tunneling occurs under positive bias, while step tunneling occurs under negative bias. Therefore, the current in the MIIM structure flows through resonant or step tunneling depending on the bias polarity. These different tunneling mechanisms rely mainly on the insulating material used and on variations in dielectric thickness. In resonant tunneling, as shown in the diagram of Figure 1c, a quantum well exists between two insulators. When the Fermi level of the metal electrode rises and reaches the lowest energy level of the well, electrons tunnel from the first metal to the second metal through the insulating layers via the quantum well. However, as shown in Figure 1d, in step tunneling, an electron tunnels through only the wider-band-gap insulator. The tunnelling distance decreases, which increases current density; this agrees with [35].

The performance of an MIIM tunnel diode is evaluated based on its figures of merit, which include responsivity (β), dynamic resistance (R_D), asymmetry (A), and nonlinearity (NL), defined respectively by:

$$\beta = \frac{1}{2}\,\frac{d^2I}{dV^2} \Big/ \frac{dI}{dV} \tag{2}$$

$$R_D = dV/dI \tag{3}$$

$$A = \left| I(+V)/I(-V) \right| \tag{4}$$

$$NL = \left(\frac{dI}{dV}\right)\frac{V}{I} \tag{5}$$

The simulation was performed using a quantum mechanical simulator in MATLAB, based on [40]. The materials properties needed for the simulation are the metal's work function, the electron affinities of the insulating layers used, their dielectric constants, electron effective masses, and thicknesses. As electron effective masses in SnO_2 and Al_2O_3, we assumed 0.3m_0 [41] and 0.75m_0 respectively. The dielectric constant used for SnO_2, was 9.6 [42], while 8 was chosen for Al_2O_3. Table 2 summarizes the material parameters used in the simulation.

2.2 | Fabrication

Figure 2a–h illustrates the different steps for fabricating the MIIM diode device. The substrate is rinsed in deionized (DI) water,

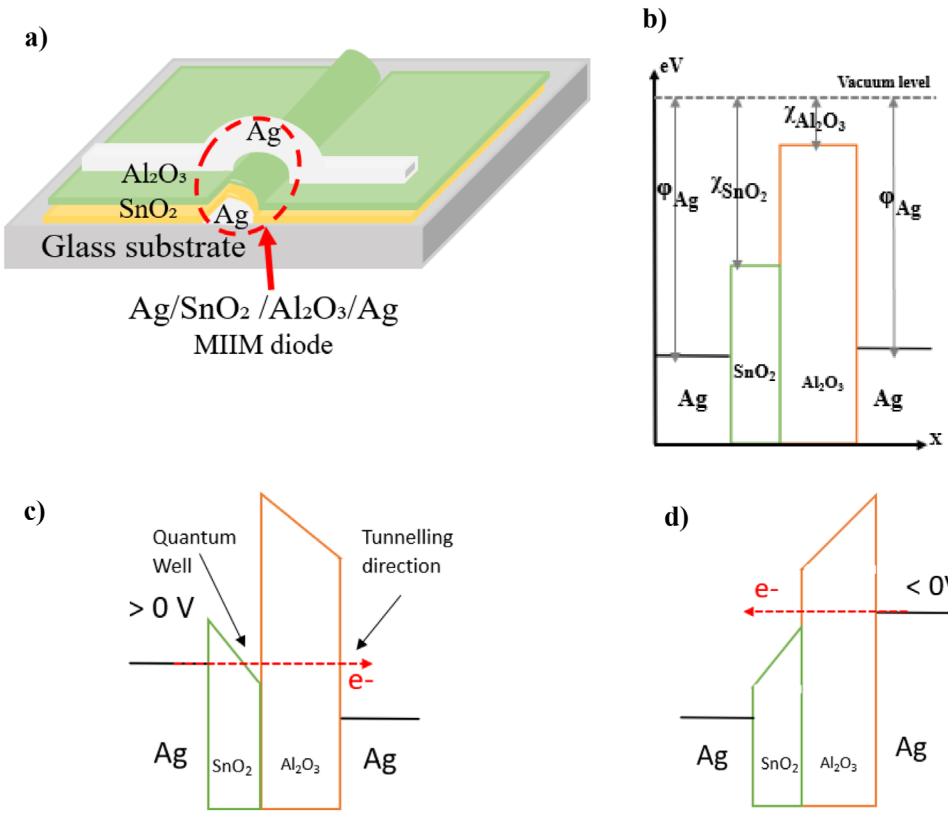

FIGURE 1 | (a) schematic structure of the printed $Ag/SnO_2/Al_2O_3/Ag$ MIIM diode, (b) energy band diagram of the MIIM structure, resonant tunneling in (c) forward bias, and (d) reverse bias.

TABLE 2 | Material parameters used in the simulation.

Material	Work function	Insulator	Electron affinity	Dielectric constant
Ag	4.7 **(eV)**	Al_2O_3	1.57 eV [43]	8
		SnO_2	4.5 eV [44, 45]	9.6 [42]

then cleaned in ultrasonic baths with acetone (ACE), followed by isopropanol (IPA) for five minutes each. It is then dried with a nitrogen gun and subjected to a plasma treatment with Argon (Ar) for three minutes to enhance the adhesion of the printed material. The fabrication process uses the XTPL delta printing system based on UPD. The Ag nanopaste (XTPL CL85), designed for this purpose, has a viscosity of at least 1000 cP and a metal content of 82 wt%. The nozzle used has an internal opening of 3.5 µm. The properties of the Ag nanopaste (CL85) are mentioned in [46] (see Table S1). The pressure is set to 9 millibars, the velocity to 0.01 mm/s, and the time delay to 100 ms. Afterward, the samples are placed on a hot plate and annealed at 150 °C for ten minutes to improve stability and conductivity. This high-viscosity Ag-based ink is formulated to explicitly suppress drooling and start–stop irregularities. The higher viscosity stabilizes the nozzle–substrate meniscus, minimizes uncontrolled ink outflow when the pneumatic pressure is released, and eliminates the formation of satellite droplets at the beginning or end of printed features. As a result, the Ag electrode has a thickness of about 200 nm and a width of 5 µm, measured with a Bruker Dektak XT profilometer (see Figure S3b). Then, a cross line is printed on each bottom electrode, facilitating further DC contacts and measurement pads. Before applying insulators to the bottom lines, the ends of the printed line are covered with a Kapton tape to avoid deposition of the insulation layer on top (Figure 2c). Subsequently, a 1 nm layer of SnO_2 is deposited on the desired surface, followed by a 1 nm layer of Al_2O_3, using ALD. During the SnO_2 deposition, the substrate temperature remains at 90 °C. The precursor source, Tetrakis(dimethylamino) tin (IV) (TDMASn), is kept at 70 °C, while the H_2O source stays at 18 °C. The pulse and purge times for TDMASn are 1.6 s and 5.0 s, respectively, with a 90 sccm flow of N_2. For H_2O, the pulse and purge times are 1.0 s and 5.0 s, with 90 sccm N_2. A total of 10 *ALD cycles is performed to create the 1 nm SnO_2 layer, based on a deposition rate of 1 nm per 10 cycles. For the Al_2O_3 layer, the substrate temperature remains at 90 °C. Trimethylaluminum (TMA) and H_2O are used as precursors and reactants, maintained at 18 °C. The pulse and purge times for TMA are 0.2 and 10.0 s, respectively, with a 200 sccm N_2 flow. For H_2O, the same pulse and purge times and N_2 flow rate are applied. A total of 8 ALD cycles is used to deposit the 1 nm Al_2O_3 layer. The Kapton tape is then removed (Figure 2f), and the top electrode is printed under the same conditions as the bottom electrode to form the $Ag/SnO_2/Al_2O_3/Ag$ MIIM diode. It is important to note that printing the top electrode is a delicate process. When positioning the nozzle near the insulating layer, special care should be taken to prevent damage and avoid short circuits. In a final step, aerosol jet printing is used to contact the UPD-deposited silver lines and to offer measurement pads for the electrical characterization.

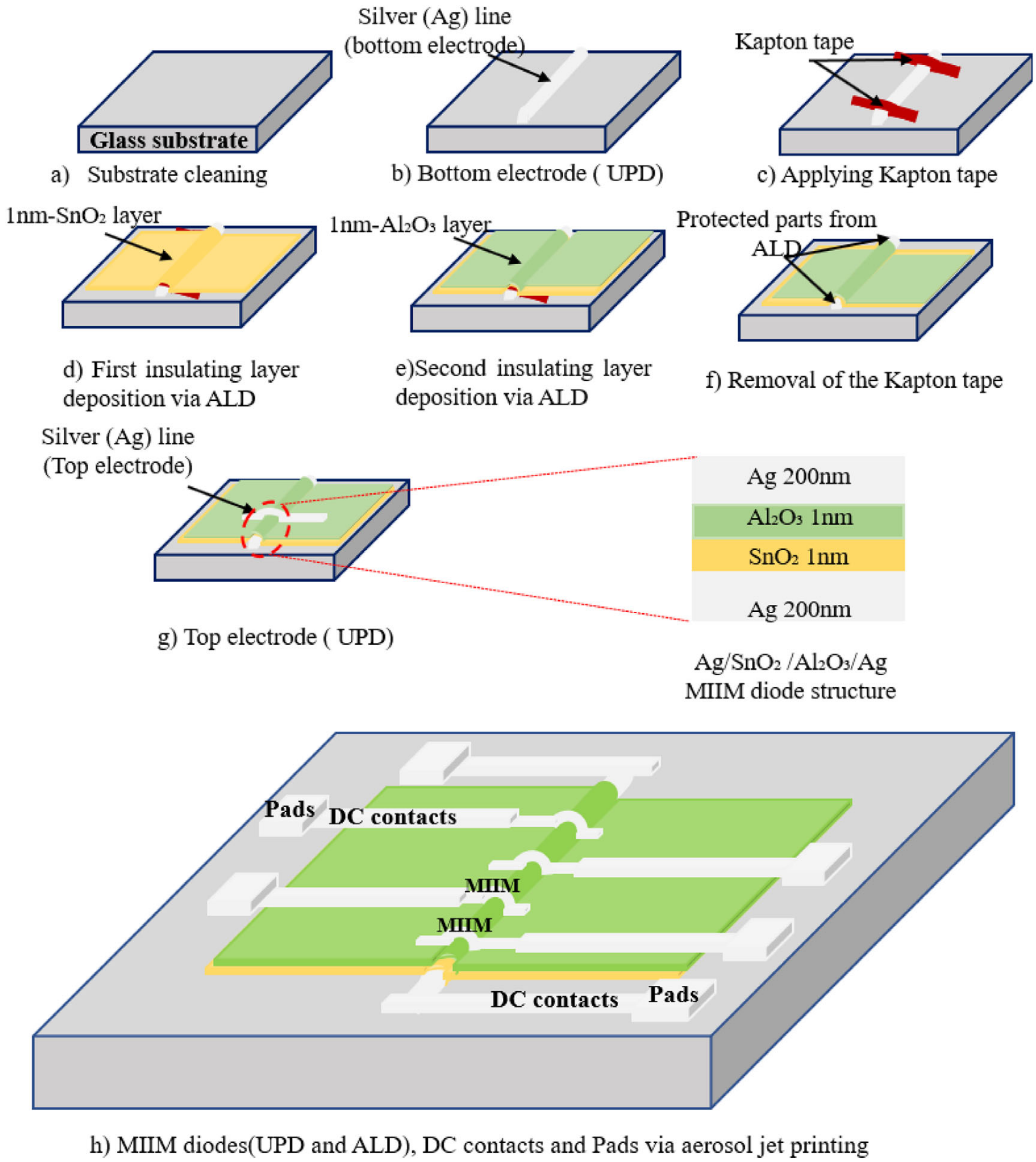

FIGURE 2 | Fabrication process of the Metal-Insulator-Insulator-Metal (MIIM) diode using ultraprecise dispensing techniques: (a) Substrate cleaning; (b) Bottom electrode placement (ultraprecise dispensing with XTPL delta printing system); (c) Applying Kapton tape before depositing insulators; (d) and (e) Depositing the first and second insulating layers via ALD; (f) Removing the Kapton tape; (g) Cross section of the bottom electrode showing the MIIM diode structure (Ag/SnO_2/Al_2O_3/Ag); (h) Complete structure with MIIM diodes, DC contacts, and pads created through aerosol jet printing.

This fabrication process for the MIIM diodes was repeated (cf. Figure S1). In the same vein, the I/V-measurement protocol is repeated to assess measurement stability and bias-stress effects (see Figure S4).

2.3 | Electrical Characterization

Figure 3 shows a photo of the fabricated MIIM devices. A Keithley 2450 source meter measured the I/V characteristics with 4-probe configurations to reduce parasitic resistance from the contacts and cables. Voltage sweeps ranged from −600 to +600 mV in 50 mV steps. Figure 3b,c shows light microscope images of the diodes and the connections between DC contacts and pads. The overlap structure and contact area of the MIIM diode are shown. Figure 3d displays an FIB-SEM image of the reported MIIM diode. The diode's active area is determined to be 5.4 µm × 4 µm.

3 | Results and Discussion

3.1 | MIIM Diode Simulation and Optimization

MIIM diode simulation and optimization were conducted to identify the best parameters before fabrication, aiming to enhance device performance. This approach helps avoid trial-and-error during the experimental phase by guiding accurate, efficient

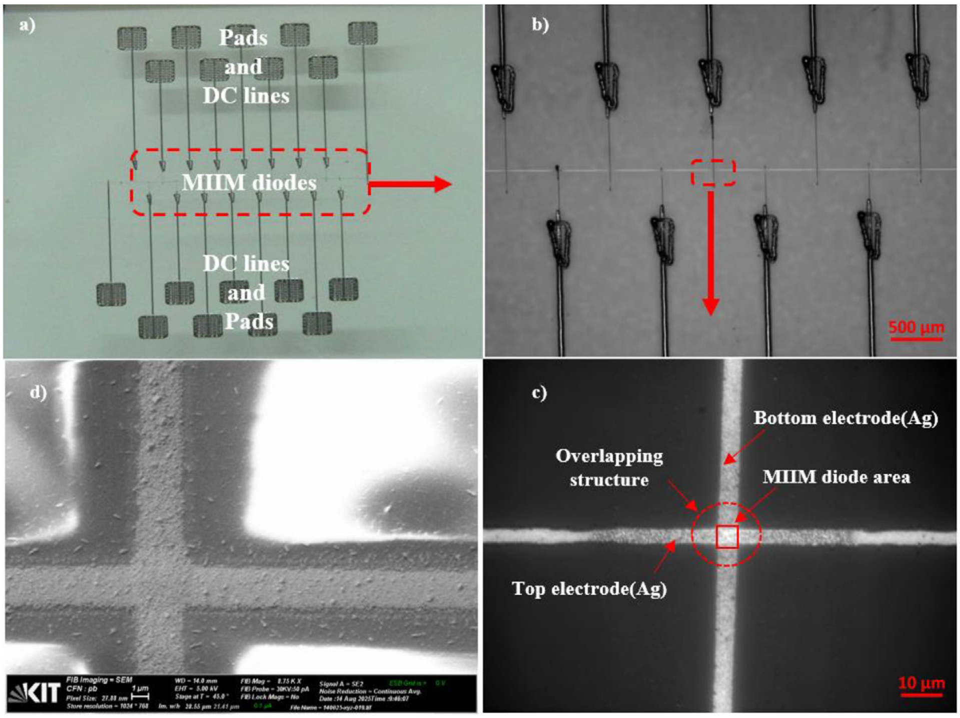

FIGURE 3 | The photo of the printed MIIM diodes, showing the pads and DC lines, includes: (a) the complete device; (b) and (c) light microscope images of the MIIM diode overlapping structure and diode area; and (d) the FIB-SEM image of the printed MIIM structure with a diode area of 5.4 µm × 4 µm.

fabrication. A simulation of combining the two insulating layers was conducted to find the optimal thickness. Figure 4 displays the tunneling current for different thickness combinations between SnO_2 and Al_2O_3. Various combinations were tested with a maximum thickness of 3 nm for each, increasing in 1 nm steps. As expected, and shown in Figure 4a–c, we observe that as the thickness of the insulating layers increases, the tunnel current decreases. A thicker insulator widens the potential barrier electrons must tunnel through. The tunneling probability decreases exponentially with increasing barrier width. However, compared to Figure 4d–f, it is evident that the tunnel current is more sensitive to the thickness of Al_2O_3, which acts as a perfect insulating layer, than to that of SnO_2. These insulators present distinct electronic properties. Al_2O_3 acts as a high-quality, wide-bandgap insulator with a relatively high electron barrier height. Therefore, increasing its thickness strongly suppresses electron tunneling. However, SnO_2 has a lower effective barrier height. Consequently, variations in SnO_2 thickness have a less pronounced impact on the tunneling current compared to Al_2O_3. Indeed, this behavior is explained by the MIIM structures, as shown in the energy band diagram in Figure 1b. On the other hand, Al_2O_3 presents the highest tunneling barrier; thus, it is the layer that controls and dominates the tunneling in the stack. Therefore, small changes in its thickness can cause significant variations in current, whereas thickness variations in SnO_2 have a smaller effect on current. The tunneling current decreases as the insulator thickness increases because the tunneling probability depends exponentially on the barrier width, and it is more sensitive to Al_2O_3 thickness because Al_2O_3 creates a higher and more effective tunneling barrier than SnO_2. The tunnel current is decreased from the pico- to femto-ampere range when the Al_2O_3 thickness exceeds 1 nm, based on a diode active area of 4 µm × 4 µm. The tunnel current increases by about one order of magnitude when increasing the SnO_2 thickness from 1 nm while keeping the Al_2O_3 thickness at 1 nm (Figure 4d). This behavior can be explained by voltage-dependent resonance that enables tunneling. However, we observe a decrease in the current by eight orders of magnitude when increasing the Al_2O_3 thickness from 1 nm (Figure 4a) to 3 nm. Therefore, since the efficiency of an MIIM diode depends on its ability to exhibit high responsivity and low resistance at zero-bias voltage for use in a rectenna, we evaluated the zero-bias dynamic resistance and responsivity for each thickness combination of insulating layers. The results are shown in Figure 5. It can be seen from this figure that, in general, high responsivity corresponds to high resistance. However, 1 nm of Al_2O_3 combined with 2 nm of SnO_2 shows a zero-bias dynamic resistance of 4.9×10^7 Ω and a responsivity of 0.69 A/W. In comparison, 2 nm of Al_2O_3 combined with 1 nm of SnO_2 exhibits a much higher resistance of 2.6×10^{14} Ω and a lower responsivity of 0.22 A/W. By interchanging the thicknesses of Al_2O_3 and SnO_2, the zero-bias dynamic resistance decreases by seven orders of magnitude, and the responsivity increases by 204%. The same phenomenon is observable with 2 nm of Al_2O_3 and 3 nm of SnO_2. Thus, when the thickness difference between Al_2O_3 and SnO_2 is 2 nm, specifically, 1 nm of Al_2O_3 and 3 nm of SnO_2, the resistance decreases by fourteen orders of magnitude, and the responsivity increases by 473%. With a priority on a small resistance, the optimal combination is 1 nm of SnO_2 and 1 nm of Al_2O_3 (SnO_2(1 nm)/Al_2O_3(1 nm)). Consequently, these insulating layer thicknesses have been realized in diode fabrication using the ALD process, as explained in section 2.2.

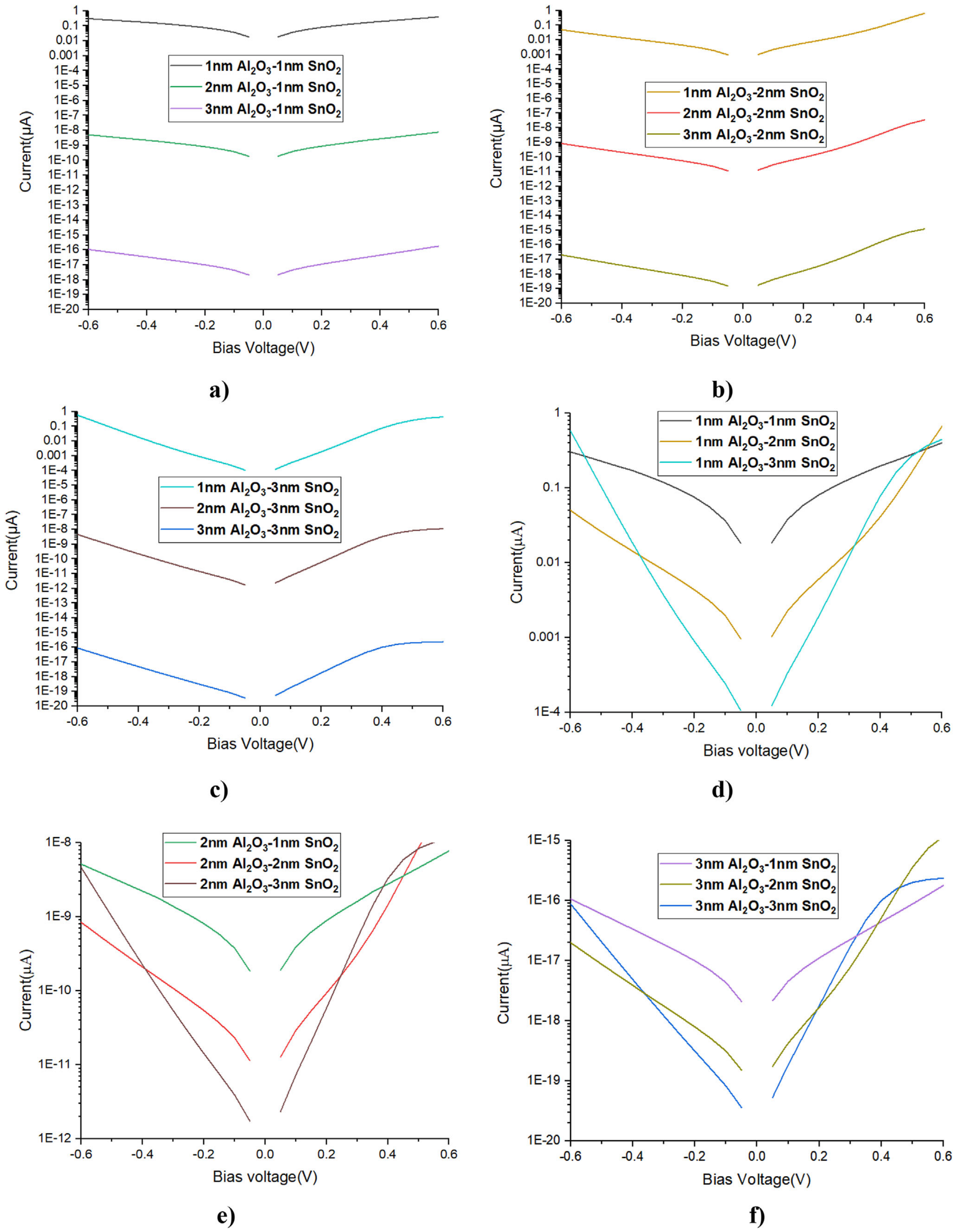

FIGURE 4 | Tunnel current versus bias voltages with various insulating layer thickness combinations of SnO_2 and Al_2O_3.

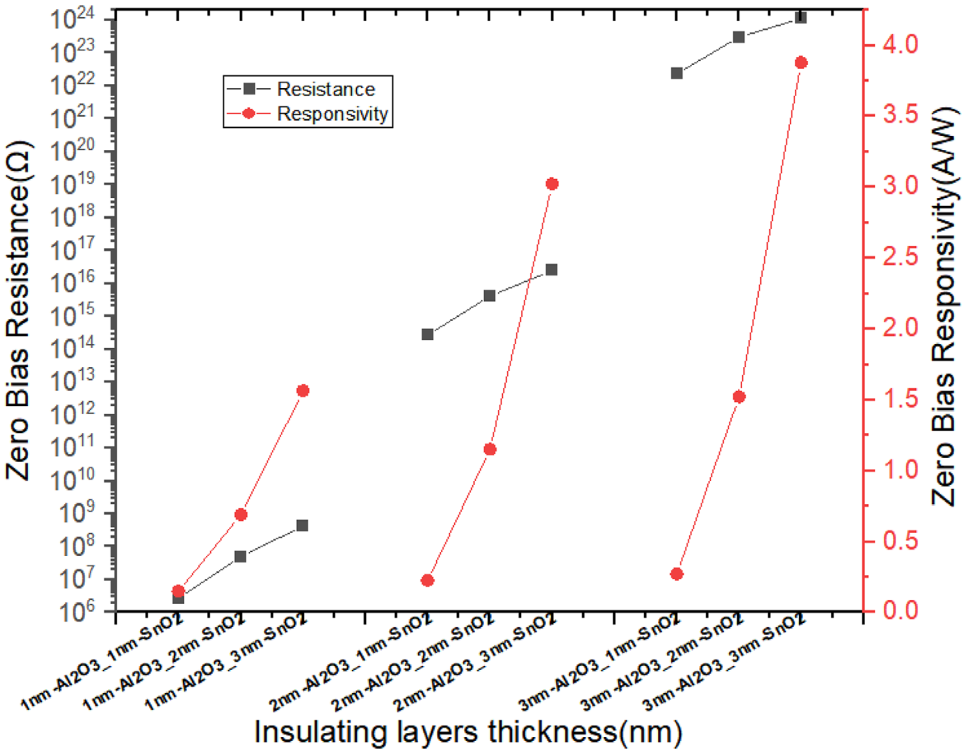

FIGURE 5 | Zero-bias resistance and responsivity for different combinations of insulating layer thicknesses of SnO_2 and Al_2O_3.

3.2 | DC Characterization

Figure 6a,b displays the measured I-V characteristics of the $Ag/SnO_2/Al_2O_3/Ag$ MIIM diode on a semilogarithmic (Figure 6a) and a linear scale (Figure 6b), featuring a 5^{th}-order polynomial fit and a quantum simulator calculation. The figure shows that the measured tunneling current, as described theoretically by Equation (1), ranges from nanoamperes to microamperes. This matches results reported in [11, 31, 47], which involve multiple insulators placed between similar and dissimilar electrodes. The figure shows good agreement between the measured and simulated data. The diode's active area was maintained at 5.4 µm × 4 µm, based on values obtained from the FIB-SEM image. The thicknesses of the insulating layers obtained from fitting the simulations and measured data are 0.905 nm for Al_2O_3 and 0.97 nm for SnO_2, based on the parameters in Table 2. These values are slightly below the nominal ALD values due to fluctuations in the deposition rate. A fifth-order polynomial fit was applied to the measured I-V characteristics to extract the diode parameters. The diode performance parameters, including responsivity, dynamic resistance, asymmetry, and nonlinearity, were extracted from Figure 6 using Equations 2–4 mentioned above. These parameters were then calculated and plotted in Figure 7a–d to illustrate the diode's figures of merit. As a result, the printed $Ag/SnO_2/Al_2O_3/Ag$ MIIM diode shows a zero-bias responsivity of $\beta_0 = -1.13$ A/W and a dynamic resistance of $R_D = 39.56$ kΩ. An improvement in the figures of merit is evident in Table 1, which compares previous studies on metal-insulator(s)-metal diodes fabricated using various techniques. Although silver (Ag) is used for both the bottom and top electrodes, slight asymmetry and nonlinearity are still observed, as shown in Figure 7c,d. The chemical stability and wide bandgap (Eg = 3.6 eV [42]) of SnO_2, combined with Al_2O_3, an effective insulator deposited using ALD, indicate an asymmetrical barrier that reduces leakage current and improves rectification. Indeed, the ALD is recognized as one of the most effective techniques for nanoscale layer deposition, as demonstrated in [12, 48, 49]. This method allows the formation of well-defined, conformal layers with low roughness and a pinhole-free structure. Such high-quality deposition ensures excellent adhesion of the insulating layers sandwiched between the bottom and top electrodes. Therefore, increasing the number of different insulating layers reduces leakage current and enhances rectification [50]. However, increasing the total thickness of the insulating stack also increases the dynamic resistance [50]. As mentioned and supported by [50], an asymmetric potential barrier is obtained by combining two different insulating layers. Specifically, the SnO_2/Al_2O_3 bilayer creates three distinct metal–insulator interfaces within the MIIM diode, each exhibiting a different barrier height (Figure 1b). The electron affinities of ALD-deposited SnO_2 and Al_2O_3 are 4.5 eV (χ_1) and 1.57 eV (χ_2), respectively, while the Ag work function is $\varphi 1 = 4.7$ eV. The resulting barrier heights are calculated as follows: $\varnothing_1 = \varphi_1$-$\chi_1$ = 0.2 eV, $\varnothing_2 = \chi_1$-χ_2 = 2.93 eV, and $\varnothing_3 = \varphi_1$-$\chi_2$ = 3.13 eV. The shape of the energy band diagram also changes when a bias is applied to the metallic electrodes. When a positive bias is applied, the probability of an electron tunnelling from left to right increases more than for the case of a negative bias and the tunnelling from right to left (Figure 1c,d).

4 | Conclusions

This work introduces a new fabrication method for metal–insulator–metal (MIM) diodes that uses printing rather than traditional lithography. The printing method uses direct ink

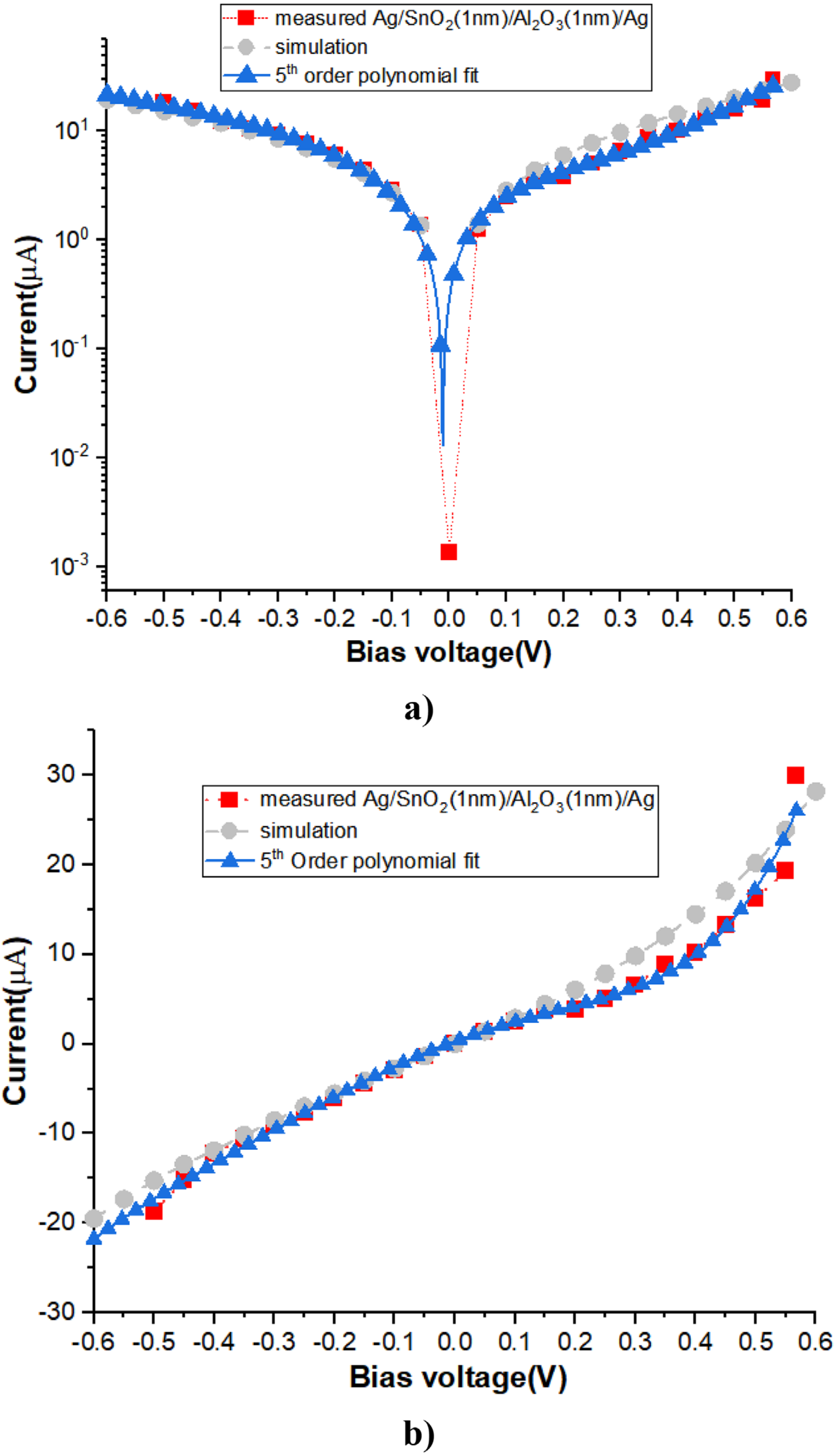

FIGURE 6 | I-V characteristics of $Ag/SnO_2/Al_2O_3/Ag$ MIIM diode measured, simulated, and fitted with a 5th-order polynomial; (a) semilogarithmic and (b) linear scale.

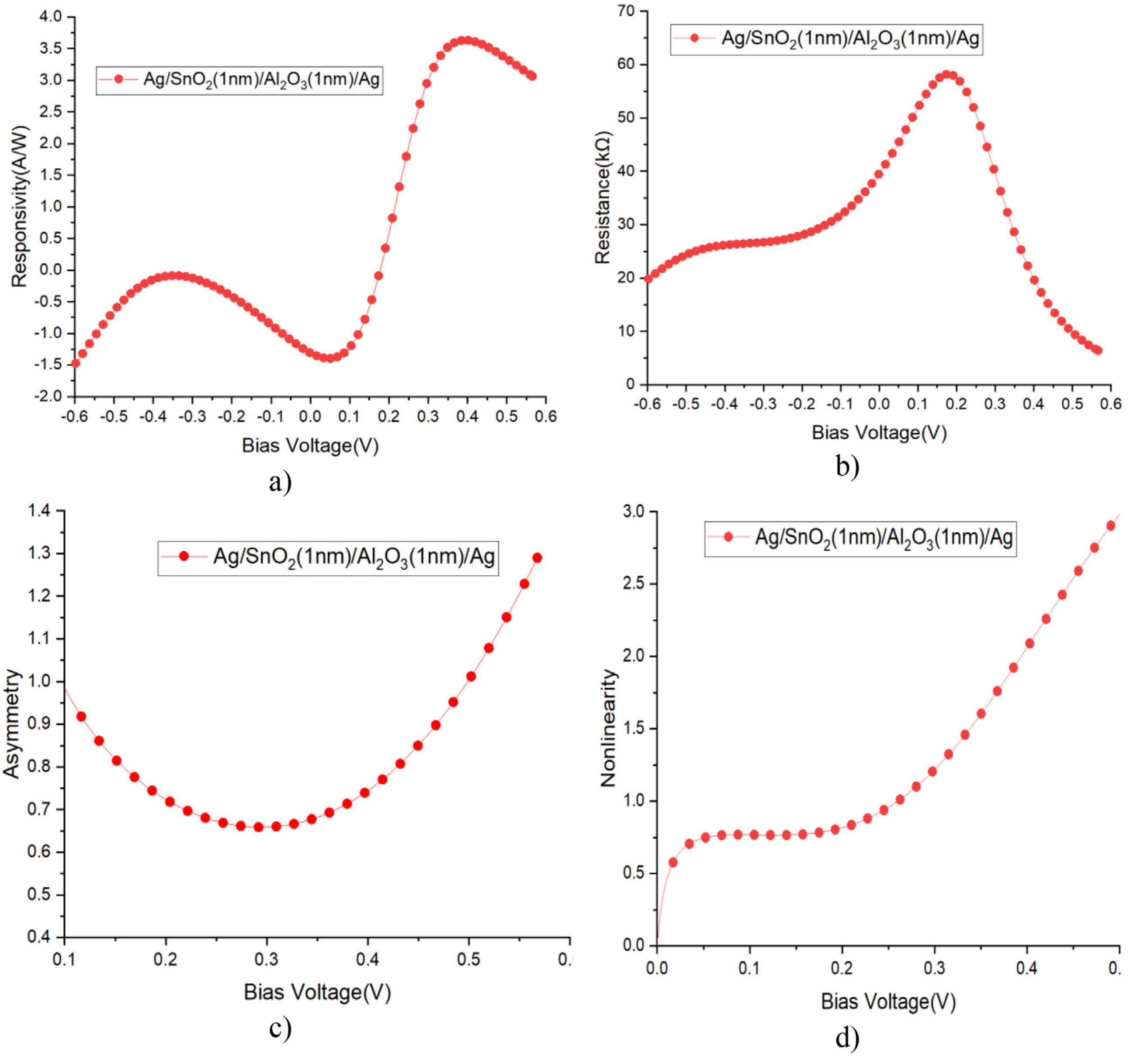

FIGURE 7 | Extracted rectification parameters for the printed Ag/SnO_2/Al_2O_3/Ag MIIM diode: (a) responsivity, (b) dynamic resistance, (c) asymmetry, and (d) nonlinearity as functions of bias voltage.

writing (DIW), which enables precise deposition, reducing material waste and increasing fabrication efficiency. Ultra-precise dispensing (UPD) is used to print the bottom and top electrodes of the MIIM diode, while the insulating layers comprising 1 nm of SnO_2 and 1 nm of Al_2O_3 are deposited by atomic layer deposition (ALD). This results in an overlapping structure (Ag/SnO_2/Al_2O_3/Ag). The printed Ag/SnO_2/Al_2O_3/Ag MIIM diode shows a tunneling current in the microampere range, a zero-bias responsivity of $\beta_0 = -1.13$ A/W, and a dynamic resistance of RD = 39.56 kΩ. An asymmetry and nonlinearity of approximately 0.99 and 2.98 at 0.6 V are observed. The measured data agree with simulations based on the WKB method. This method simplifies the fabrication process for MIM-diodes on a large area as needed for, for example, energy harvesting and other applications. Furthermore, the compatibility of the UPD technique with flexible and non-planar substrates further expands the potential for wearable electronics, smart textiles, and embedded IoT devices. Overall, this work provides a practical, manufacturable route to high-frequency rectification components. Furthermore, it will establish the technological groundwork for future commercial rectenna-based energy-harvesting and sensing solutions.

Acknowledgements

This work was supported by the Partnership for Skills in Applied Sciences, Engineering and Technology (PASET)- Regional Scholarship and Innovation Fund (RSIF).

Open access funding enabled and organized by Projekt DEAL.

Conflicts of Interest

The authors declare no conflicts of interest.

Data Availability Statement

The data that support the findings of this study are available from the corresponding author upon reasonable request.

References

1. D. Matsuura, M. Shimizu, Z. Liu, and H. Yugami, "Optical Rectenna with Wide Wavelength Coverage from a Hollow Resonator Coupled with a Metal–Insulator–Metal Tunnel Diode," *Applied Physics Express* 15, no. 6 (2022): 062001.

2. M. Kowalski and M. Kastek, "Comparative Studies of Passive Imaging in Terahertz and Mid-Wavelength Infrared Ranges for Object Detection," *IEEE Transactions on Information Forensics and Security* 11, no. 9 (2016): 2028–2035.

3. M. Dagenais, K. Choi, F. Yesilkoy, A. N. Chryssis, and M. C. Peckerar, "Solar Spectrum Rectification Using Nano-Antennas and Tunneling Diodes," *Optoelectron Integr Circuits XII* 7605, no. 1 (2010): 129–140.

4. I. Nemr Noureddine, N. Sedghi, J. S. Wrench, I. Z. Mitrovic, P. R. Chalker, and S. Hall, "Structural and Electrical Investigation of MI2M and MI3M Diodes for Improved Non-Linear, Low Bias Rectification," *Solid-State Electronics* 194 (2022): 108349.

5. G. Jayaswal, A. Belkadi, A. Meredov, B. Pelz, G. Moddel, and A. Shamim, "Optical Rectification through an Al2O3 Based MIM Passive Rectenna at 28.3 THz," *Materials Today Energy* 7 (2018): 1–9.

6. S. Kang and E. A. B. Eltahir, "North China Plain Threatened by Deadly Heatwaves due to Climate Change and Irrigation," *Nature Communications* 9, no. 1 (2018): 2894.

7. A. Savadogo, T. N. Nyangonda, B. O. Aduda, U. Lemmer, and M. Hussein, "Characteristics of a V-Shaped Rectenna for 28.3 THz Energy Harvesting," *Journal of Computational Electronics* 24, no. 2 (2025): 59.

8. A. Y. Elsharabasy, A. H. Alshehri, M. H. Bakr, M. J. Deen, K. P. Musselman, and M. Yavuz, "Near Zero-Bias MIIM Diode Based on TiO_2/ZnO for Energy Harvesting Applications," *AIP Advances* 9, no. 11 (2019): 115207.

9. E. G. Arsoy, M. Inac, A. Shafique, M. Ozcan, and Y. Gurbuz, "The Metal-Insulator-Metal Diodes for Infrared Energy Harvesting and Detection Applications," *InInfrared Technology and Applications XLII* 9819 (2016): 93–97.

10. M. N. Gadalla, M. Abdel-Rahman, and A. Shamim, "Design, Optimization and Fabrication of a 28.3 THz Nano-Rectenna for Infrared Detection and Rectification," *Scientific Reports* 4 (2014): 4270.

11. F. Aydinoglu, M. Alhazmi, B. Cui, O. M. Ramahi, M. Irannejad, and M. Yavuz, "Higher Performance Metal-Insulator-Metal Diodes Using Multiple Insulator Layers," *Austin Journal of Nanomedicine & Nanotechnology* 1, no. 1 (2013): 2–4.

12. N. Alimardani, J. M. McGlone, J. F. Wager, and J. F. Conley, "Conduction Processes in Metal–Insulator–Metal Diodes with Ta_2O_5 and Nb_2O_5 Insulators Deposited by Atomic Layer Deposition," *Journal of Vacuum Science & Technology A* 32, no. 1 (2014): 01A122.

13. N. Alimardani, E. William Cowell, J. F. Wager, J. F. Conley, D. R. Evans, M. Chin, S. J. Kilpatrick, and M. Dubey, "Impact of Electrode Roughness on Metal-Insulator-Metal Tunnel Diodes with Atomic Layer Deposited Al_2O_3 Tunnel Barriers," *Journal of Vacuum Science & Technology A* 30, no. 1 (2012): 01A113.

14. S. Krishnan, E. Stefanakos, and S. Bhansali, "Effects of Dielectric Thickness and Contact Area on Current–Voltage Characteristics of Thin Film Metal–Insulator–Metal Diodes," *Thin Solid Films* 516, no. 8 (2008): 2244–2250.

15. A. Yahyaoui, A. Elsharabasy, J. Yousaf, K. Sedraoui, and H. Rmili, "MIIM-based Optical Log Spiral Rectenna for Efficient IR Energy Harvesting," *Alexandria Engineering Journal* 61, no. 11 (Nov.2022): 8897–8909.

16. E. Donchev, L. Technologies, J. S. Pang, P. M. Gammon, and A. E. R. Centeno, "The Rectenna Device : From Theory to Practice (a Review)," *MRS Energy & Sustainability 1, 1* (2014), https://doi.org/10.1557/mre.2014.6.

17. D. Gao and J. G. Zhou, "Designs and Applications of Electrohydrodynamic 3D Printing," *International Journal of Bioprinting* 5, no. 1 (2019): 172.

18. K. Skarżyński and M. Słoma, "Printed Electronics in Radiofrequency Energy Harvesters and Wireless Power Transfer Rectennas for IoT Applications," *Advanced Electronic Materials* 9, no. 8 (2023): 2300238.

19. A. Wiatrowska, P. Kowalczewski, K. Fiączyk, Ł. Witczak, J. Gadzalińska, M. Łysień, L. Schneider, Ł. Kosior, and F. Granek, "59-3: Ultra-Precise Printing of Micrometer-Size Interconnectors for High-Resolution MicroLED Displays," *SID Symposium Digest of Technical Papers* 52, no. 1 (2021): 833–836.

20. P. Kowalczewski, A. Wiatrowska, and M. Dusza, "Novel Approach to Print Submicron Conductive Lines: From the Fundamental Process to the Laboratory Printer, " in *2018 International Flexible Electronics Technology Conference (IFETC)*, Ottawa, ON, Canada, (2018), pp. 1–2, https://doi.org/10.1109/IFECT.2018.8583842.

21. A. Zumeit, A. S. Dahiya, and R. Dahiya, "Printed Silicon Nanoribbon-Based Temperature Sensors on Flexible Substrates," *IEEE Sensors Letters* 9, no. 6 (2025): 1–4.

22. M. Roemhild, G. Gramlich, H. Baur, T. Zwick, and N. Fruehauf, "Ultraprecise Printing of D-Band Transmission Lines," *IEEE Microwave and Wireless Technology Letters* 33, no. 10 (2023): 1419–1422.

23. A. Wiatrowska, K. Fiączyk, and J. Gadzalińska, "Ultraprecise Deposition of Micrometer-Size Conductive Features for Advanced Packaging, " in *2022 IEEE 72nd Electronic Components and Technology Conference (ECTC)*, IEEE, San Diego, CA, USA, (2022), pp. 1573–1576, https://doi.org/10.1109/ECTC51906.2022.00251.

24. S. Almalki, S. B. Tekin, N. Sedghi, S. Hall, and I. Z. Mitrovic, "Applicability of Sc2O3 versus Al2O3 in MIM Rectifiers for IR Rectenna," *Solid-State Electronics* 184 (2021): 108082.

25. K. Choi, F. Yesilkoy, G. Ryu, S. H. Cho, N. Goldsman, M. Dagenais, and M. Peckerar, "A Focused Asymmetric Metal–Insulator–Metal Tunneling Diode: Fabrication, DC Characteristics and RF Rectification Analysis," *IEEE Transactions on Electron Devices* 58, no. 10 (2011): 3519–3528.

26. S. B. Tekin, A. D. Weerakkody, N. Sedghi, S. Hall, M. Werner, J. S. Wrench, P. R. Chalker, and I. Z. Mitrovic, "Single and Triple Insulator Metal-Insulator-Metal Diodes for Infrared Rectennas," *Solid-State Electronics* 185 (2021): 108096.

27. M. F. Zia, M. R. Abdel-Rahman, N. F. Al-Khalli, and N. A. Debbar, "Fabrication and Characterization of Vanadium/Vanadium Pentoxide/Vanadium (V/V2O5/V) Tunnel Junction Diodes," *Acta Physica Polonica A* 127, no. 4 (2015): 1289–1291.

28. A. D. Weerakkody, N. Sedghi, I. Z. Mitrovic, H. van Zalinge, I. Nemr Noureddine, S. Hall, J. S. Wrench, P. R. Chalker, L. J. Phillips, R. Treharne, and K. Durose, "Enhanced Low Voltage Nonlinearity in Resonant Tunneling Metal–Insulator–Insulator–Metal Nanostructures," *Microelectronic Engineering* 147 (2015): 298–301.

29. A. H. Alshehri, H. Asgarimoghaddam, L.-V. Delumeau, V. H. Nguyen, A. Ali, M. Aljaghtham, A. Alamry, D. Ozyigit, M. Yavuz, and K. P. Musselman, "Combinatorial Optimization of Metal-Insulator-Insulator-Metal (MIIM) Diodes With Thickness-Gradient Films via Spatial Atomic Layer Deposition," *Advanced Electronic Materials* 10 (2024): 2400093.

30. N. Li, C. Zhao, X. Li, P. Zhao, B. Zheng, and G. Gao, "Efficient Metal Concave Bow Tie Rectifying Antenna for Solar Energy Collection," *Optics Communications* 546 (2023): 129814.

31. S. Mizojiri, K. Shimamura, Y. Hayashi, Y. Kataoka, M. Matsukura, K. Fujiwara, and M. Yamazaki, "Metal–Insulator–Insulator–Insulator–Metal Diode Combining Defect-Enhanced Direct Tunneling and Geometric Field Enhancement," *Japanese Journal of Applied Physics* 64, no. 5 (2025): 051001.

32. S. Abrar, M. B. Hanif, A. S. Alghamdi, A. Khaliq, K. S. Abdel Halim, T. Subhani, M. Motola, and A. F. Khan, "Synthesis and Characterization of Nanostructured Multi-Layer Cr/SnO2/NiO/Cr Coatings Prepared via E-Beam Evaporation Technique for Metal-Insulator-Insulator-Metal Diodes," *Materials* 15 (2022): 3906.

33. P. Esfandiari, G. Bernstein, P. Fay, et al., "Tunable Antenna-Coupled Metal-Oxide-Metal (MOM) Uncooled IR Detector," *Infrared Technology and Applications* 5783 (2005): 470–482.

34. E. C. Kinzel, R. L. Brown, J. C. Ginn, B. A. Lail, B. A. Slovick, and G. D. Boreman, "Design of an MOM Diode-Coupled Frequency-Selective Surface," *Microwave and Optical Technology Letters* 55, no. 12 (2013): 2611–2615.

35. M. Rahman, "Tin Oxide thin Films for the Future: A Paradigm Shift in Property Engineering for Advanced Functional Devices," *Next Materials* 9 (2025): 101341.

36. Z. H. Bakr, Q. Wali, J. Ismail, N. Kumar, A. Uddin, and R. Jose, "Synergistic Combination of Electronic and Electrical Properties of SnO2 and TiO2 in a Single SnO2-TiO2 Composite Nanofiber for Dye-Sensitized Solar Cells," *Electrochimica Acta* 263 (2018): 524–532.

37. J. W. Elam, D. A. Baker, A. J. Hryn, A. B. F. Martinson, M. J Pellin, and J. T. Hupp, "Atomic Layer Deposition of Tin Oxide Films Using Tetrakis(dimethylamino) Tin," *Journal of Vacuum Science & Technology A* 252 (2025): 244–252.

38. G. A. E. Vandenbosch and Z. Ma, "Upper Bounds for the Solar Energy Harvesting Efficiency of Nano-Antennas," *Nano Energy* 1, no. 3 (2012): 494–502.

39. G. Moddel and S. Grover, *Rectenna Solar Cells* (Springer, 2013).

40. S. Grover and G. Moddel, "Engineering the Current–Voltage Characteristics of Metal–Insulator–Metal Diodes Using Double-Insulator Tunnel Barriers," *Solid-State Electronics* 67, no. 1 (2012): 94–99.

41. K. J. Button, C. G. Fonstad, and W. Dreybrodt, "Determination of the Electron Masses in Stannic Oxide by Submillimeter Cyclotron Resonance," *Physical Review B* 4, no. 12 (1971): 4539–4542.

42. M. Batzill and U. Diebold, "The Surface and Materials Science of Tin Oxide," *Progress in Surface Science* 79, no. 2–4 (2005): 47–154.

43. I. Z. Mitrovic, A. D. Weerakkody, N. Sedghi, J. F. Ralph, S. Hall, V. R. Dhanak, Z. Luo, and S. Beeby, "Controlled Modification of Resonant Tunneling in Metal-Insulator-Insulator-Metal Structures," *Applied Physics Letters* 112, no. 1 (2018): 012902.

44. O. Bierwagen, M. E. White, M. Y. Tsai, T. Nagata, and J. S. Speck, "Non-Alloyed Schottky and Ohmic Contacts to As-Grown and Oxygen-Plasma Treated n-Type SnO 2 (110) and (101) Thin Films," *Applied Physics Express* 2, no. 10 (2009): 106502.

45. F. Hossein-Babaei, S. Moghadam, and S. Masoumi, "Forming Ohmic Ag/SnO_2 Contacts," *Materials Letters* 141 (2015): 141–144.

46. M. Łysień, Ł. Witczak, A. Wiatrowska, et al., "High-Resolution Deposition of Conductive and Insulating Materials at Micrometer Scale on Complex Substrates," *Scientific Reports* 12, no. 1 (2022): 9327.

47. P. Maraghechi, A. Foroughi-Abari, K. Cadien, and A. Y. Elezzabi, "Observation of Resonant Tunneling Phenomenon in Metal-Insulator-Insulator- Insulator-Metal Electron Tunnel Devices," *Applied Physics Letters* 100, no. 11 (2012): 113503.

48. S. M. George, "Atomic Layer Deposition: An Overview," *Chemical Reviews* 110, no. 1 (2010): 111–131.

49. R. W. Johnson, A. Hultqvist, and S. F. Bent, "A Brief Review of Atomic Layer Deposition: From Fundamentals to Applications," *Materials Today* 17, no. 5 (2014): 236–246.

50. I. Z. Mitrovic, S. Almalki, S. B. Tekin, N. Sedghi, P. R. Chalker, and S. Hall, "Oxides for Rectenna Technology," *Materials* 14, no. 18 (2021): 5218.

Supporting Information

Additional supporting information can be found online in the Supporting Information section.

Supporting File: aelm70272-sup-0001-SuppMat.docx.